Bandwidth Control and Symmetry Breaking in a Mott-Hubbard Correlated Metal

Lishai Shoham,* Maria Baskin, Tom Tiwald, Guy Ankonina, Myung-Geun Han, Anna Zakharova, Shaked Caspi, Shay Joseph, Yimei Zhu, Isao H. Inoue, Cinthia Piamonteze, Marcelo J. Rozenberg, and Lior Kornblum*

In Mott materials strong electron correlation yields a spectrum of complex electronic structures. Recent synthesis advancements open realistic opportunities for harnessing Mott physics to design transformative devices. However, a major bottleneck in realizing such devices remains the lack of control over the electron correlation strength. This stems from the complexity of the electronic structure, which often veils the basic mechanisms underlying the correlation strength. This study presents control of the correlation strength by tuning the degree of orbital overlap using picometer-scale lattice engineering. This study illustrates how bandwidth control and concurrent symmetry breaking can govern the electronic structure of a correlated $SrVO_3$ model system. This study shows how tensile and compressive biaxial strain oppositely affect the $SrVO_3$ in-plane and out-of-plane orbital occupancy, resulting in the partial alleviation of the orbital degeneracy. The spectral weight redistribution under strain is derived and explained, which illustrates how high tensile strain drives the system toward a Mott insulating state. Implementation of such concepts can push correlated electron phenomena closer toward new solid-state devices and circuits. These findings therefore pave the way for understanding and controlling electron correlation in a broad range of functional materials, driving this powerful resource for novel electronics closer toward practical realization.

1. Introduction

Recent advancements in the synthesis of high-quality films and heterostructures of correlated electron materials open promising avenues toward their application in new types of functional devices.[1] One of the most attractive implementations remains the Mott field effect transistor, dubbed as the MottFET,[2–4] where the vision is to use an external stimulus, such as an electric field, to drive a Mott material across a metal to insulator transition (MIT). However, these promises have yet to be realized in practical scenarios. The development of efficient tuning mechanisms for these materials will increase their technological potential and contribute to the development of Mott devices such as the MottFET.

Correlated materials are a class of materials where strong electron correlations, defined as the ratio U/W between the electron Coulomb repulsion energy (U) and the width of the one-electron band (W), dictates the electronic structure. Sufficiently strong

L. Shoham, M. Baskin, G. Ankonina, S. Caspi, L. Kornblum
Andrew and Erna Viterbi Department of Electrical and Computer Engineering
Technion – Israel Institute of Technology
Haifa 3200003, Israel
E-mail: lishai@campus.technion.ac.il; liork@technion.ac.il
T. Tiwald
J. A. Woollam Co., Inc.
645 M Street, Suite 102, Lincoln, NE 68508, USA

M.-G. Han, Y. Zhu
Condensed Matter Physics and Materials Science
Brookhaven National Laboratory
Upton, NY 11793, USA
A. Zakharova, C. Piamonteze
Swiss Light Source
Paul Scherrer Institute
Villigen PSI CH-5232, Switzerland
S. Joseph
Rafael Ltd.
P.O. box 2250, Haifa 3102102, Israel
I. H. Inoue
National Institute of Advanced Industrial Science and Technology (AIST)
Central 5, Tsukuba 305–8565, Japan
M. J. Rozenberg
Université Paris-Saclay
CNRS
Laboratoire de Physique des Solides
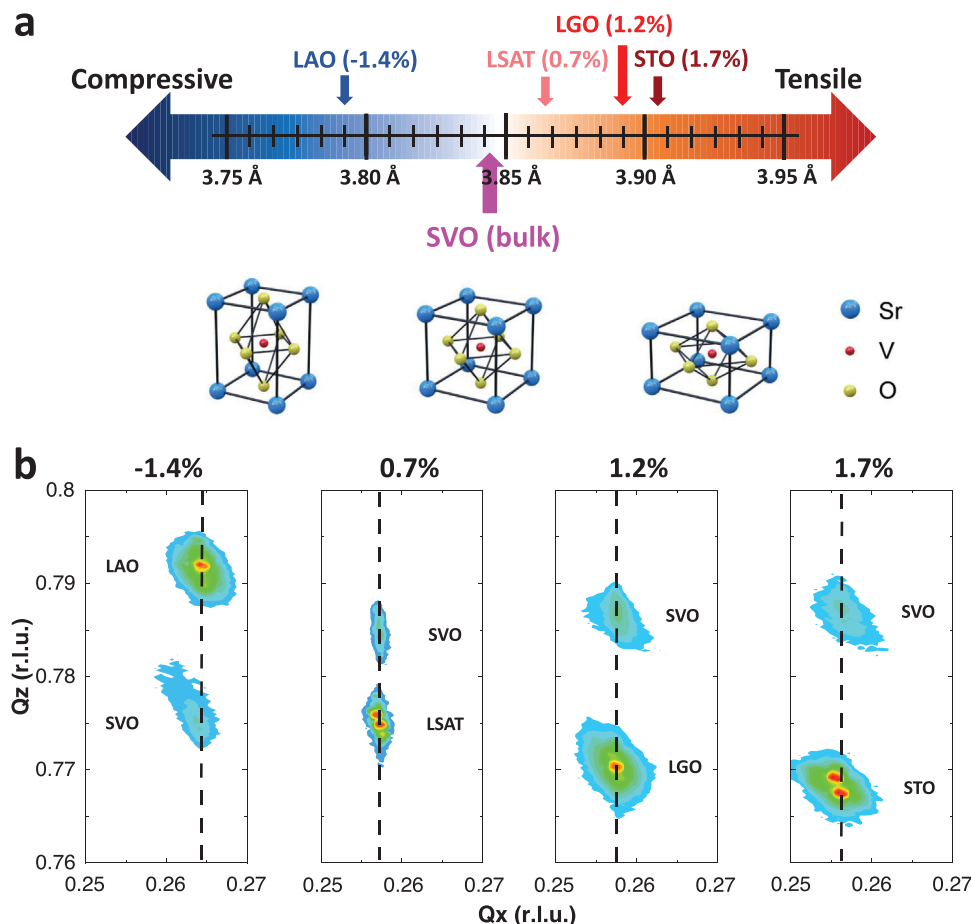Orsay 91405, France

Figure 1. a) Comparison of the (cubic/pseudocubic) lattice parameters of (bulk) SrVO$_3$ (SVO) and the various substrates used in this study to strain it: SrTiO$_3$ (STO), LaGaO$_3$ (LGO), (LaAlO$_3$)$_{0.3}$(Sr$_2$TaAlO$_6$)$_{0.7}$ (LSAT), and LaAlO (LAO). b) Reciprocal space maps (RSMs) of the strained SVO films grown on different substrates indicate coherent growth. All measurements were taken in the cubic/pseudocubic [0 1 3] orientation.

electron correlation can result in a formation of the lower and upper Hubbard bands (LHB, UHB, respectively), by transferring spectral weight from the vicinity of the Fermi level. Increasing the electron correlation strength, therefore, can drive an integer-filling Mott-Hubbard material toward a Mott insulating state.[5–8] In the intermediate state, when U/W ≈1, the LHB and UHB can coexist with the remaining spectral weight around the Fermi level, termed the quasiparticle (QP) peak.

Bandwidth control is an attractive route for tuning the electronic structure of correlated materials by changing the hopping amplitude of the carriers, determined by the degree of orbital overlap.[5] This concept can be realized by structural distortions of the unit cell, e.g., by applying chemical[9] or hydrostatic[10] pressure, or via epitaxial strain.[11–15] For example, in the Ca$_{1-x}$Sr$_x$VO$_3$ system, the value of x controls the V–O–V bond angle without changing the vanadium valance state, which was shown to result in bandwidth modulation.[16,17] In the case of epitaxial strain, the asymmetric nature of the structural distortion typically results in orbital symmetry breaking between the in-plane and out-of-plane orbitals.

Transition metal oxides provide a rich playground for correlated electron phenomena, particularly for Mott physics. SrVO$_3$ (SVO) has been a long-time prototype of strongly correlated metals owing to its relative simplicity; this is due to its cubic perovskite structure, paramagnetism, and the single valence electron in the V-3d band.[8,18–23] As predicted by theoretical studies[24,25] and shown by spectroscopy,[25–28] the V-3d band for SVO presents a three-peak structure consisting of the LHB, QP peak and UHB. Nevertheless, as a correlated metal, most of its spectral weight is located around the QP peak. Recent improvements in thin film growth methods[29–31] open the door for new possibilities, such as extending early bandwidth control attempts to a biaxial landscape.

The effect of biaxial epitaxial strain on the electronic landscape of SVO consists of two key contributions, as predicted by theory.[7] On the one hand, structural changes in the unit cell decrease (increase) the in-plane hopping amplitude under tensile (compressive) strain. An opposite effect occurs in the out-of-plane direction (**Figure 1**a). On the other hand, symmetry breaking induces a crystal field split, partially alleviating the degeneracy of the V-3d t$_{2g}$ orbitals, which constitute the backbone of the t$_{2g}$ sub-bands of the V-3d band. The degeneracy removal reduces the number of bands available for electron delocalization at the ground state,[32,33] regardless of the applied strain. Thus, under tensile strain, the concomitant contributions are expected to increase the correlation strength. Conversely, for

compressive strain, these contributions counteract each other, and the effect on the correlation strength is expected to be small. Altogether, biaxial strain is a powerful knob for controlling the electronic structure. However, the complexity of many systems often obscures the underlying mechanisms behind the correlation strength, which may explain why experimental realization of these concepts remains challenging.

In this study, we directly control the electron correlation strength of SVO by manipulation of the V–O bond length via biaxial epitaxial strain. Leaning on the theoretical foundations and predictions of Ref. [7], we start by confirming the V–O bond length modulation and strain-selective crystal field splitting (sections 2.1 and 2.2, respectively). We then apply optical conductivity analysis to illustrate how the hopping amplitude and crystal-field splitting variation reshape the electronic structure (section 2.3). We rule out any octahedral rotation using atomic resolution imaging and electron diffraction (section 2.4). The choice of the simple SVO as a model allowed us to obtain a clear picture of these concurrent effects, paving the way to generalize the results to a broad range of more complex systems.

2. Results and Discussion

2.1. Bond-Length Modulation

Epitaxial strain, which stems from a mismatch between the film and substrate, can tune the SVO electronic structure by mechanical modulation of the V–O bond length. To understand these mechanisms, we grew epitaxial SVO films (nominally 25–30 nm thick) on the following substrates: $SrTiO_3$ with 1.7% mismatch (STO, 1.7%), $LaGaO_3$ (LGO, 1.2%), $(LaAlO_3)_{0.3}(Sr_2TaAlO_6)_{0.7}$ (LSAT, 0.7%), and $LaAlO_3$ (LAO, −1.4%). The mismatch is defined as $100\% \cdot (a_{sub} - a_{SVO})/a_{sub}$, where a_{sub} and a_{SVO} are the bulk (or pseudocubic) lattice parameters of the substrate and SVO, respectively (Figure 1a). Bulk (or unstrained) SVO has a lattice parameter of 3.843 Å,[18] and a positive (negative) mismatch value translates to tensile (compressive) strain in this notation. The films exhibit high crystalline quality (Figure S1, Supporting Information) and low defect densities, evident by the high residual resistivity ratio (RRR) ranging from 4.5 to 15.3 (Figure S2, Supporting Information). Reciprocal space maps (RSMs, Figure 1b) confirm that all films are fully strained to their substrates. Thus, the nominally cubic SVO unit cell undergoes tetragonal distortion under the biaxial in-plane epitaxial strain applied by the substrate.

From the structural analysis, we conclude that the V–O bond length directly manifests the biaxial in-plane strain (octahedral rotations are ruled out in section 2.4). Under tensile strain, the in-plane V–O bond length increases, reducing the V $3d$ – O $2p$ orbital overlap and decreasing the hopping amplitude. The opposite occurs for compressive strain, where the strain-induced bond length shortening increases the orbital overlap. We note that strain can also be accommodated by defect formation, to be further discussed in Section 2.4, Figure S1 (Supporting Information) and discussion therein. Unlike several other ABO_3 systems that exhibit octahedral rotations, where the B–O–B bond angle governs the hopping amplitude,[17] in the present study it is controlled solely via the bond length variation. The bandwidth (W) is proportional to the hopping amplitude; thus, controlling the hopping amplitude is a straightforward and powerful tool to shape the electronic structure of correlated materials.

2.2. Symmetry Breaking of the V-3d t$_{2g}$ States

In addition to bandwidth control, the strain-induced tetragonal distortion increases the correlation strength via crystal-field splitting.[7,34,35] The unstrained SVO $3d^1$ system has threefold degenerate t_{2g} states at the ground state (d_{xy}, d_{xz}, d_{yz}). Under compressive (tensile) strain, the out-of-plane (in-plane) states, d_{xz}/d_{yz} (d_{xy}), are stabilized (**Figure 2**a). Namely, for a fixed integer occupation of n = 1, where n is the number of electrons per site, the number of degenerate bands (N) in the ground state is reduced from N = 3 for an unstrained SVO, to N = 2 or N = 1 for compressive and tensile strained SVO, respectively. This reduction in N, namely the reduction of the available delocalized states, is expected to increase the correlation strength for both strain types.[7]

To establish this strain-induced partial alleviation of the SVO t_{2g} degeneracy, we employ x-ray linear dichroism (XLD) measurements at the V $L_{2,3}$ edge. The samples were measured with two different x-ray linear polarizations: i) parallel to the film's plane ($I_∥$) and ii) at 30° from the film's normal ($I_⊥$, for simplicity), where most of the signal originates from the perpendicular polarization (Figure 2b). The measured signals, $I_∥$ and $I_⊥$, are roughly proportional to the corresponding in-plane and out-of-plane unoccupied states. Therefore, XLD, defined as the difference between the two intensities ($I_⊥ - I_∥$), is sensitive to any preferred occupation in the system. As shown in Figure 2c, the XLD signal exhibits a remarkable mirror inversion between compressive (SVO-LAO) and tensile (SVO-LSAT, SVO-STO) strain states, indicating the expected inverse orbital occupation between biaxial tensile and compressive strain.

The XLD qualitative comparison demonstrates how the application of biaxial strain controls the SVO preferred occupation. In other words, the energy lowering of the d_{xy} (tensile) or the d_{xz}/d_{yz} (compressive) states is governed by the tetragonal distortion. These findings are in line with previous works demonstrating strain-controlled preferred occupation in other systems.[36–38] While theoretically predicted for SVO,[39] to our knowledge, this is the first experimental demonstration of strain-controlled preferred occupation of a Mott-Hubbard system, providing direct evidence of the straightforward control over the electronic structure.

2.3. Strain Effect on the Electronic Structure

We now address the question; how does the concurrent modulation of the hopping amplitude and the crystal field splitting govern the correlation strength? For compressive strain, we expect the contributions of the hopping amplitude increase to counteract the crystal field split (N = 3→2), altogether exhibiting a negligible contribution to the correlation strength and the electronic structure. Conversely, for tensile strain, we expect both contributions to increase the correlation strength, and drive the system toward its insulating state.

To elucidate how the correlation strength is affected by the epitaxial strain, we study the electronic structure by employing optical conductivity analysis.[40–42] The frequency-dependent optical
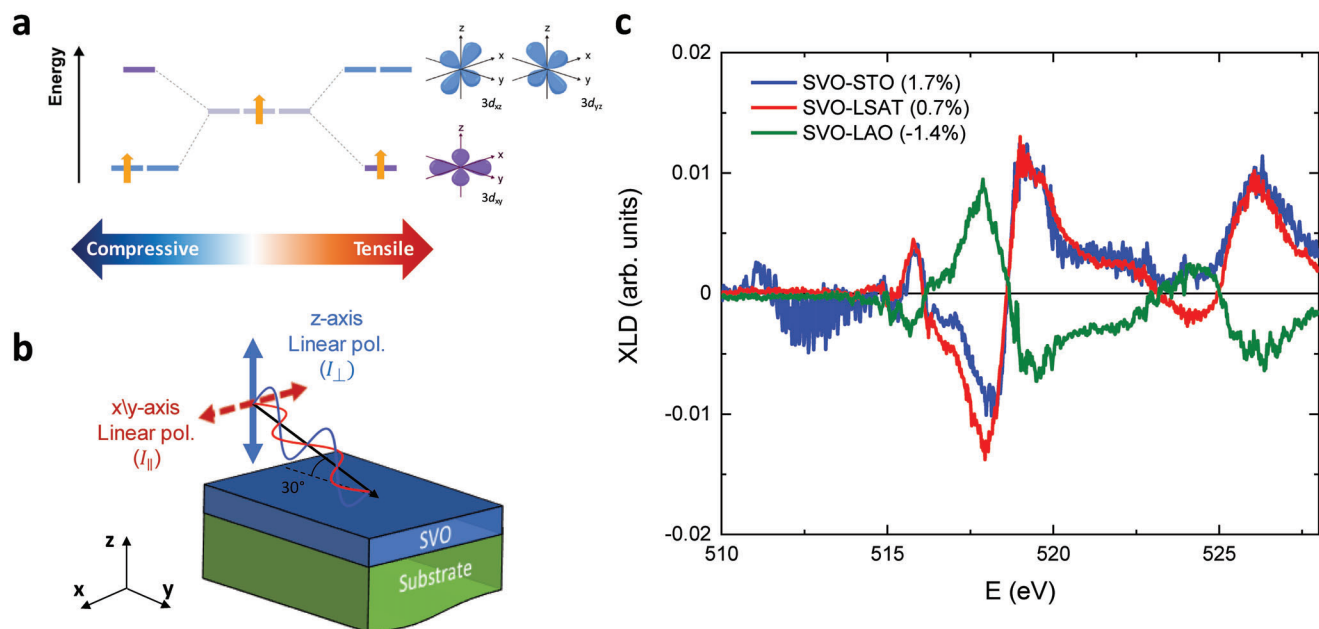
**ADVANCED
SCIENCE NEWS**

www.advancedsciencenews.com

**ADVANCED
FUNCTIONAL
MATERIALS**

www.afm-journal.de

Figure 2. Strain control of the preferred orbital occupation. a) Schematic plot of the $3d^1$ t_{2g} states under both signs of biaxial strain. b) Schematic illustration of the x-ray absorption measurement at two linear polarizations. The grazing angle between the x-ray beam and the xy plane is 30°. Thus, $I_\parallel$ probes the in-plane orbitals, while $I_\perp$ probes mainly the out-of-plane orbitals, with a small component of the in-plane. c) Normalized x-ray linear dichroism (XLD) calculated as $I_\perp - I_\parallel$ acquired in x-ray excited optical luminescence (XEOL) mode at the V $L_{2,3}$ edge. The x-ray absorption spectroscopy (XAS), defined as $I_\perp + I_\parallel$, and the data analysis are discussed in the Supporting Information and presented in Figures S3 and S4, respectively.

conductivity is calculated from the complex dielectric function using the relation[43] $\sigma(\omega) = -i\epsilon_0[\epsilon(\omega) - 1]\omega$, where ω is the frequency, ϵ_0 is the vacuum dielectric constant, and ϵ is the complex dielectric function (extracted from spectroscopic ellipsometry measurements,[44] Figure S5, Supporting Information). To a first approximation, the real part of the optical conductivity (hereafter referred to as the optical conductivity) is proportional to ex-

citations within the single-particle spectral weight of the band structure.[45] The optical conductivity spectrum can thus be used to understand the spectral weight redistribution stemming from the correlation strength modulation.

The optical conductivity of the strained SVO films is presented in **Figure 3**a (and Figure S6, Supporting Information). We note that the ellipsometric measurement is primarily sensitive to
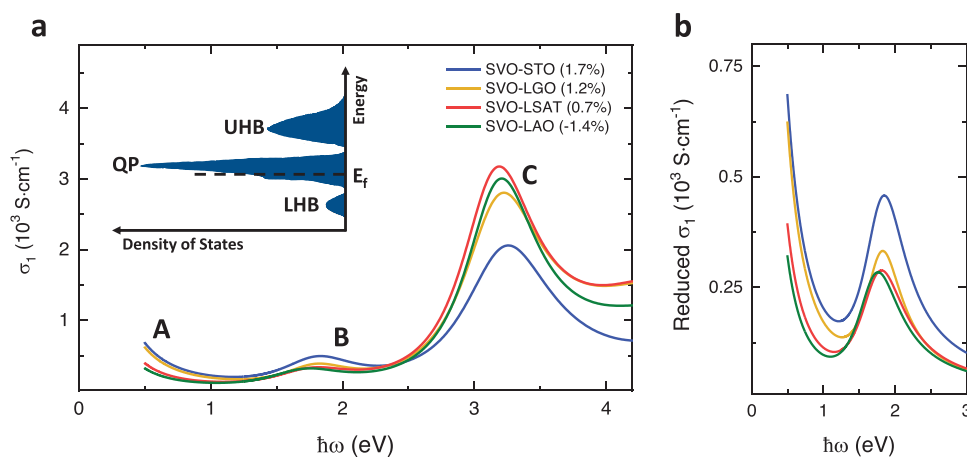

Figure 3. a) Room temperature optical conductivity of SVO under tensile and compressive strain. The metallic spectra exhibit a Drude tail (peak A), a weak feature attributed to the U/2 energy (peak B), and a large feature stemming from the charge transfer (CT) excitations (peak C). Peak C may also contain U excitations, but their overall weight will be negligible (see text). The inset shows a schematic illustration of the SVO V-3d density of states featuring the QP peak and the Hubbard bands. b) Reduced optical conductivity, composed of only excitations within the V-3d band (peaks A + B). We subtracted the CT contribution by eliminating their corresponding oscillators from the imaginary part of the dielectric function. Additional information is available in the Supporting Information and Figures S8 and S9 therein.

ADVANCED
SCIENCE NEWS
www.advancedsciencenews.com

ADVANCED
FUNCTIONAL
MATERIALS
www.afm-journal.de

in-plane properties, especially for the low thickness (<30 nm) of the films reported here. Therefore, the optical conductivity analysis addresses mainly the in-plane strain effect. We assign the features to the known electronic structure of SVO to reveal the role of strain. The Drude peak (peak A) originates from the metallicity of the SVO films, corresponding to intraband transitions of the valence electrons within the conduction band of the V-3d states. The extrapolated conductivity at $\omega = 0$ and the optical mobility are similar to the measured dc conductivity and Hall mobility (Figure S7a,b, Supporting Information, respectively), further validating the optical analysis. The effective mass of the strained SVO films (Figure S7c, Supporting Information), as extracted from the Drude peak (see Supporting Information for details), exhibits an increase going from compressive to tensile strain, attesting to the expected increase in correlation strength.

As a correlated metal, the SVO 3d band presents a three-peak structure (Figure 3a inset, following Ref. [24]) featuring additional excitations. As measured and theorized earlier,[17,41,45] the optical conductivity spectra consist of two additional transitions within the V-3d band: i) at about U/2 energy (at ≈1.8 eV) corresponding to the transition from the occupied LHB (O-LHB) to unoccupied QP states, and from occupied QP states to the unoccupied UHB (UO-UHB), and ii) at the U energy (≈3.5 eV) corresponding to the transition from the O-LHB to the UO-UHB. Thus, we assign the weak feature at ≈1.9 eV (peak B) to the expected U/2 excitation energy, where we ascribe it mainly to excitations from the O-LHB to the UO-QP peak, due to the high spectral weight of the latter. In addition, the SVO O 2p states are calculated to be ≈3 eV below the Fermi level,[7,24] resulting in a charge-transfer (CT) excitation energy of ≈3.5 eV for O 2p →V 3d transitions.[41] Therefore, the feature at ≈3.2 eV (peak C) can stem from both U and CT transitions; however, owing to the high O 2p spectral weight, the CT feature will overshadow the U peak, making it the prominent component of this feature.

Having explained the optical spectra, we now address the strain-dependent spectral weight evolution. We highlight the distinct change in peaks B and C intensities as the SVO approaches the highest tensile strain (SVO-STO, 1.7%). While the intensity of peak C decreases with increasing strain, the intensity of peak B increases (as illustrated in Figure 3b). This behavior can be explained by spectral weight redistribution of the 3d band, where the incoherent LHB and UHB spectral weights increase at the expense of the coherent QP peak, as the SVO approaches the Mott insulating state. Hence, tensile strain is shown to increase the SVO correlation strength. We emphasize that this spectral weight redistribution is governed by the magnitude of the biaxial tensile strain, causing a concurrent hopping amplitude decrease and crystal field splitting. Our observation of spectral weight reduction with increasing tensile strain around ≈3.2 eV agrees with a previous work, where chemical pressure (Ca substitution) was applied as means to control the bandwidth.[17]

Therefore, utilizing epitaxial strain as a control parameter, the spectral weight can be moved around the Mott landscape in a thin-film scenario, which is important for device implementation. This approach highlights a useful tuning parameter for leveraging Mott physics for new electronic devices, driving them closer toward practical realization.

2.4. Tetragonal Distortion Without Octahedral Rotation

Some perovskites will accommodate the epitaxial strain via rotation of the BO_6 octahedra in addition to changes in the atomic bond distances.[46] If octahedral rotation occurs, the in-plane hopping parameter decreases (increases) under compressive (tensile) strain due to the distortion of the B–O–B bond angle.[16] Conversely, here the strain is expected to induce a modulation of the atomic bond length rather than the angle. In order to rule out the bending of the V–O–V bond angle off its nominal 180°, scanning transmission electron microscopy (STEM) is employed. High-angle annular dark-field (HAADF, **Figures 4**a,b) and annular bright-field (ABF, Figure 4c) STEM images along the [100] direction are shown for a compressively strained SVO film (SVO-LAO, −1.4%). The results indicate no systematic shift of the V columns along the out-of-plane direction. The electron diffraction pattern of the SVO film is shown in the inset of Figure 4b, where half-integer diffractions are absent, further validating the real-space linear bond observation. A similar observation is made for tensile strained SVO film (SVO-LSAT, 0.7%), as presented in Figure S10 (Supporting Information). Furthermore, using a similar approach, Wang et al. ruled out octahedral rotations for an SVO film on an STO substrate (SVO-STO, 1.7%).[47]

In addition to ruling out octahedral tilts or rotations in the strained SVO films, the STEM analysis further confirms the expected tetragonal distortion in real-space. The strain-induced tetragonal distortion of the unit cell is observed for SVO-LAO via the distortion of the VO_6 octahedra. We measured four inner angles of the oxygen octahedra (designated as O1, O2, O3, and O4). It can be seen that the two horizontal angles (O2 and O4) are larger than the two vertical angles (O1 and O3). The average angle of O1 and O3 is 85.4 ± 2.3°, whereas the average angle of O2 and O4 is 94.5 ± 1.9°. These inner octahedron angles are comparable to those calculated using the tetragonal lattice parameters (Table S1, Supporting Information), which are 88.8° for O1 and O3, and 91.2° for O2 and O4.

We note an additional possible strain accommodation mechanism, by the formation of defects such as vacancies and dislocations. However, the high structural quality and RRR values (see Supporting Information for details) suggest that the small possible concentration of defects carries a negligible effect onto the SVO electronic properties.

3. Conclusion

SVO provides a simple testbed for electron correlation. We harnessed this simplicity to derive a clear picture of the effect of biaxial strain on the correlation strength and the resulting electronic structure. Using a thorough structural analysis, we show that in this nominally-cubic system, epitaxial strain directly translates to V-O bond length modulation via tetragonal distortion without changing the V–O–V bond angle. In addition to variation of the hopping amplitude, the bond length modulation also results in crystal field splitting of the nominally-degenerate V-3d t_{2g} orbitals; both contributions are considered to concurrently affect the correlation strength and the V-3d band structure. The change in correlation strength is manifested in the SVO V-3d band spectral weight redistribution, observed by optical conductivity. Tensile strain is shown to further drive the system
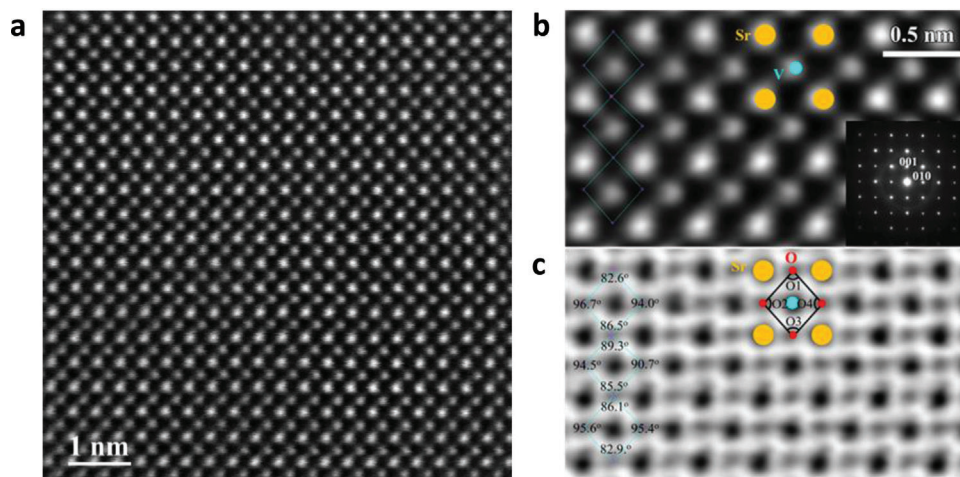
ADVANCED
SCIENCE NEWS
www.advancedsciencenews.com

ADVANCED
FUNCTIONAL
MATERIALS
www.afm-journal.de

Figure 4. Cross-section high-resolution STEM micrographs of a compressively strained SVO film on an LAO substrate, imaged with HAADF a) and b), and ABF c) along the [100] zone axis. The electron diffraction pattern is shown in the inset of (b), showing the absence of half-integer diffractions. Oxygen octahedral angles are evaluated from the ABF STEM image (see Experimental for details).

toward an insulating state, a consequence of the increased correlation strength. We thus demonstrate a straightforward approach for modulating the electronic structure of this correlated model system. Applying these methods to more complex systems, particularly near an electronic phase transition, is expected to yield robust effects and large changes in the electronic structure, providing an efficient tuning parameter for harnessing correlated materials and Mott physics toward novel practical solid state electronic devices and circuits.

4. Experimental Section

Sample Preparation: SVO films (60 u.c.) were epitaxially grown on (001)-oriented (cubic/pseudocubic) LAO, LSAT, STO, and LGO substrates (CrysTec GmbH). This thickness was chosen to reduce the contribution of possible surface effects[48] while ensuring the coherent epitaxy of the films. The growth was done using oxide molecular beam epitaxy (MBE) at a background pressure of molecular oxygen of $\sim 5 \times 10^{-7}$ Torr and substrate (thermocouple) temperature of 1000 °C.[30] Substrate preparation is described in the Supporting Information. After growth, the samples were cooled to room temperature under the same oxygen pressure as the growth.

Structural Characterization: $2\theta/\omega$ scans and RSMs were performed with x-ray diffraction (XRD) using a Rigaku SmartLab with a two-bounce incident monochromator.

Scanning Transmission Electron Microscopy: A cross-sectional TEM sample was prepared by a focused ion beam (FIB) with Ga+ ions. The final milling was done with 5 keV Ga+ ions to reduce FIB-induced damage. A cross-sectional TEM sample with its plane normal tilted $\approx 22.5°$ from the [100] and [110] directions was prepared, which is within the tilting range of the TEM sample holder. By tilting +/− 22.5°, a set of atomic resolution images and electron diffraction patterns is obtained along both the [100] and [110] directions from the same area of the sample to examine octahedra tilts or rotations. The JEOL ARM 200CF at the Brookhaven National Laboratory, equipped with double aberration correctors, was used to obtain HAADF and ABF STEM images. The ranges of the collection angles for HAADF and ABF are 67–275 and 11–23 mrad, respectively. The convergence angle for the imaging electron beam was 21.2 mrad. Oxygen octahedra angles are measured in the ABF STEM image after refining the oxygen positions using the Oxygen Octahedra (O-O) Picker.[49] Prior to the bond angle measurement by the O-O Picker, the HAADF and ABF STEM

images were filtered by a Butterworth Filter (4th order) and an Average Background Subtraction Filter, using a Digital Micrograph script written by D. Mitchell (www.dmscripting.com).

X-ray Absorption Spectroscopy: The XAS spectra were acquired at the Swiss Light Source (SLS) on the XTreme beamline.[50] The measurements were performed using XEOL detection mode[51] under zero magnetic field in linear horizontal and vertical polarizations. The SVO-LAO and SVO-LSAT samples were measured at room temperature, while the SVO-STO sample was measured at 120°K to increase luminescence from the STO substrate.

Spectroscopic Ellipsometry (NIR+VIS+UV): Ellipsometry data was acquired using a dual rotating compensator ellipsometer (RC2 ellipsometer, J. A. Woollam Co.). Data were acquired at 1058 wavelengths from 193 to 2500 nm (0.496 to 6.425 eV), at incident angles of 55, 60, 65, 70, and 75°. Focusing attachments reduced the beam diameter to ≈ 300 μm.

Supporting Information

Supporting Information is available from the Wiley Online Library or from the author.

Acknowledgements

Conflict of Interest

The authors declare no conflict of interest.

Data Availability Statement

The data that support the findings of this study are available in the supplementary material of this article and the raw data is available as an additional xlsx file.

Keywords

correlated electrons, correlated metals, Mott materials, transition metal oxides

[1] Y. Zhou, S. Ramanathan, *Crit. Rev. Solid State Mater. Sci.* **2013**, *38*, 286.

[2] I. H. Inoue, M. J. Rozenberg, *Adv. Funct. Mater.* **2008**, *18*, 2289.

[3] J. Son, S. Rajan, S. Stemmer, S. J. Allen, *J. Appl. Phys.* **2011**, *110*, 084503.

[4] Z. Zhong, M. Wallerberger, J. M. Tomczak, C. Taranto, N. Parragh, A. Toschi, G. Sangiovanni, K. Held, *Phys. Rev. Lett.* **2015**, *114*, 246401.

[5] M. Imada, A. Fujimori, Y. Tokura, *Rev. Mod. Phys.* **1998**, *70*, 1039.

[6] M. J. Rozenberg, *Phys Rev B Condens Matter Mater Phys* **1997**, *55*, R4855.

[7] G. Sclauzero, K. Dymkowski, C. Ederer, *Phys. Rev. B* **2016**, *94*, 245109.

[8] A. Fujimori, I. Hase, H. Namatame, Y. Fujishima, Y. Tokura, H. Eisaki, S. Uchida, K. Takegahara, F. M. F. De Groot, *Phys. Rev. Lett.* **1992**, *69*, 1796.

[9] J. B. Torrance, P. Lacorre, A. I. Nazzal, E. J. Ansaldo, C. Niedermayer, *Phys. Rev. B* **1992**, *45*, 8209.

[10] P. C. Canfield, J. D. Thompson, S. W. Cheong, L. W. Rupp, *Phys. Rev. B* **1993**, *47*, 12357.

[11] W. S. Choi, H. N. Lee, *Phys Rev B Condens Matter Mater Phys* **2015**, *91*, 174101.

[12] D. G. Schlom, L. Q. Chen, C. J. Fennie, V. Gopalan, D. A. Muller, X. Pan, R. Ramesh, R. Uecker, *MRS Bull.* **2014**, *39*, 118.

[13] S. Catalano, M. Gibert, V. Bisogni, O. E. Peil, F. He, R. Sutarto, M. Viret, P. Zubko, R. Scherwitzl, A. Georges, G. A. Sawatzky, T. Schmitt, J. M. Triscone, *APL Mater.* **2014**, *2*, 116110.

[14] Y. M. Wu, Y. E. Suyolcu, G. Kim, G. Christiani, Y. Wang, B. Keimer, G. Logvenov, P. A. Van Aken, *ACS Nano* **2021**, *15*, 16228.

[15] D. Han, R. Moalla, I. Fina, V. M. Giordano, M. D'Esperonnat, C. Botella, G. Grenet, R. Debord, S. Pailhès, G. Saint-Girons, R. Bachelet, *ACS Appl. Electron. Mater.* **2021**, *3*, 3461.

[16] I. Inoue, O. Goto, H. Makino, N. E. Hussey, M. Ishikawa, *Phys. Rev. B* **1998**, *58*, 4372.

[17] H. Makino, I. H. Inoue, M. J. Rozenberg, Y. Aiura, I. Hase, S. Onari, *Phys. Rev. B* **1998**, *58*, 4384.

[18] P. Dougier, J. C. C. Fan, J. B. Goodenough, *J. Solid State Chem.* **1975**, *14*, 247.

[19] L. Zhang, Y. Zhou, L. Guo, W. Zhao, A. Barnes, H. Zhang, C. Eaton, Y. Zheng, M. Brahlek, H. F. Haneef, N. J. Podraza, M. H. W. Chan, V. Gopalan, K. M. Rabe, R. Engel-herbert, *Nat. Mater.* **2016**, *15*, 204.

[20] K. Yoshimatsu, T. Okabe, H. Kumigashira, S. Okamoto, S. Aizaki, A. Fujimori, M. Oshima, *Phys. Rev. Lett.* **2010**, *104*, 147601.

[21] M. Gu, S. A. Wolf, J. Lu, *Adv. Mater. Interfaces* **2014**, *1*, 1300126.

[22] M. Mirjolet, H. B. Vasili, Ll. López-Conesa, S. Estradé, F. Peiró, J. Santiso, F. Sánchez, P. Machado, P. Gargiani, M. Valvidares, J. Fontcuberta, *Adv. Funct. Mater.* **2019**, *29*, 1904238.

[23] M. Takizawa, M. Minohara, H. Kumigashira, D. Toyota, M. Oshima, H. Wadati, T. Yoshida, A. Fujimori, M. Lippmaa, M. Kawasaki, H. Koinuma, G. Sordi, M. Rozenberg, *Phys. Rev. B* **2009**, *80*, 235104.

[24] I. A. Nekrasov, G. Keller, D. E. Kondakov, A. V. Kozhevnikov, T. Pruschke, K. Held, D. Vollhardt, V. I. Anisimov, *Phys. Rev. B* **2005**, *72*, 155106.

[25] T. Yoshida, M. Kobayashi, K. Yoshimatsu, H. Kumigashira, A. Fujimori, *J Electron Spectros Relat Phenomena* **2016**, *208*, 11.

[26] A. Sekiyama, H. Fujiwara, S. Imada, S. Suga, H. Eisaki, S. I. Uchida, K. Takegahara, H. Harima, Y. Saitoh, I. A. Nekrasov, G. Keller, D. E. Kondakov, A. V. Kozhevnikov, T. Pruschke, K. Held, D. Vollhardt, V. I. Anisimov, *Phys. Rev. Lett.* **2004**, *93*, 156402.

[27] M. J. Rozenberg, I. H. Inoue, H. Makino, F. Iga, Y. Nishihara, *Phys. Rev. Lett.* **1996**, *76*, 4781.

[28] I. H. Inoue, I. Hase, Y. Aiura, A. Fujimori, K. Morikawa, T. Mizokawa, Y. Haruyama, T. Maruyama, Y. Nishihara, *Phys. C* **1994**, *235–240*, 1007.

[29] J. A. Moyer, C. Eaton, R. Engel-Herbert, *Adv. Mater.* **2013**, *25*, 3578.

[30] L. Shoham, M. Baskin, M. Han, Y. Zhu, L. Kornblum, *Adv. Electron. Mater.* **2019**, *6*, 1900584.

[31] M. Mirjolet, F. Sánchez, J. Fontcuberta, *Adv. Funct. Mater.* **2019**, *29*, 1808432.

[32] N. Manini, G. E. Santoro, A. Dal Corso, E. Tosatti, *Phys. Rev. B* **2002**, *66*, 115107.

[33] A. I. Poteryaev, M. Ferrero, A. Georges, O. Parcollet, *Phys. Rev. B* **2008**, *78*, 045115.

[34] T. Kita, T. Ohashi, N. Kawakami, *Phys. Rev. B* **2011**, *84*, 195130.

[35] P. Werner, E. Gull, A. J. Millis, *Phys. Rev. B* **2009**, *79*, 115119.

[36] D. Pesquera, G. Herranz, A. Barla, E. Pellegrin, F. Bondino, E. Magnano, F. Sánchez, J. Fontcuberta, *Nat. Commun.* **2012**, *3*, 1189.

[37] C. Aruta, G. Ghiringhelli, A. Tebano, N. G. Boggio, N. B. Brookes, P. G. Medaglia, G. Balestrino, *Phys. Rev. B* **2006**, *73*, 235121.

[38] P. C. Rogge, R. J. Green, P. Shafer, G. Fabbris, A. M. Barbour, B. M. Lefler, E. Arenholz, M. P. M. Dean, S. J. May, *Phys. Rev. B* **2018**, *98*, 201115(R).

[39] M. Wu, J. C. Zheng, H. Q. Wang, *Phys. Rev. B* **2018**, *97*, 245138.

[40] H. Meley, M. Tran, J. Teyssier, J. A. Krieger, T. Prokscha, A. Suter, Z. Salman, M. Viret, D. Van Der Marel, S. Gariglio, *Phys. Rev. B* **2021**, *103*, 125112.

[41] R. J. O. Mossanek, M. Abbate, P. T. Fonseca, A. Fujimori, H. Eisaki, S. Uchida, Y. Tokura, *Phys. Rev. B* **2009**, *80*, 195107.

[42] F. Inaba, T. Arima, T. Ishikawa, T. Katsufuji, Y. Tokura, *Phys. Rev. B* **1995**, *52*, R2221.

[43] H. G. Tompkins, E. A. Irene, *Handbook of Ellipsometry*, William Andrew Publishing; Springer-Verlag GmbH & Co. KG, Heidelberg, Germany **2005**.

[44] J. N. Hilfiker, N. Singh, T. Tiwald, D. Convey, S. M. Smith, J. H. Baker, H. G. Tompkins, *Thin Solid Films* **2008**, *516*, 7979.

[45] M. J. Rozenberg, G. Kotliar, H. Kajueter, G. A. Thomas, D. H. Rapkine, J. M. Honig, P. Metcalf, *Phys. Rev. Lett.* **1995**, *75*, 105.

[46] J. M. Rondinelli, N. A. Spaldin, *Adv. Mater.* **2011**, *23*, 3363.

[47] G. Wang, Z. Wang, M. Meng, M. Saghayezhian, L. Chen, C. Chen, H. Guo, Y. Zhu, E. W. Plummer, J. Zhang, *Phys. Rev. B* **2019**, *100*, 155114.

[48] S. Caspi, L. Shoham, M. Baskin, K. Weinfeld, C. Piamonteze, K. A. Stoerzinger, L. Kornblum, *J Vac Sci Technol A* **2022**, *40*, 013208.

[49] Y. Wang, U. Salzberger, W. Sigle, Y. E. Suyolcu, P. A. van Aken, *Ultramicroscopy* **2016**, *168*, 46.

[50] C. Piamonteze, U. Flechsig, S. Rusponi, J. Dreiser, J. Heidler, M. Schmidt, R. Wetter, M. Calvi, T. Schmidt, H. Pruchova, J. Krempasky, C. Quitmann, H. Brune, F. Nolting, *J Synchrotron Radiat* **2012**, *19*, 661.

[51] C. Piamonteze, Y. W. Windsor, S. R. V. Avula, E. Kirkc, U. Staub, *J Synchrotron Radiat* **2020**, *27*, 1289.